Spectral Broadening of a Single Er^{3+} Ion in a Si Nanotransistor

Jiliang Yang,[1,3] Jian Wang,[1,3] Wenda Fan,[1,3] Yangbo Zhang,[1,3] Changkui Duan,[1,3] Guangchong Hu,[4] Gabriele G. de Boo,[4] Brett C. Johnson,[5,6] Jeffrey C. McCallum,[6] Sven Rogge,[4] Chunming Yin,[1,2,3,*] and Jiangfeng Du[1,2,3]

[1] *CAS Key Laboratory of Microscale Magnetic Resonance and School of Physical Sciences, University of Science and Technology of China, Hefei 230026, China*

[2] *Hefei National Laboratory, University of Science and Technology of China, Hefei 230088, China*

[3] *CAS Center for Excellence in Quantum Information and Quantum Physics, University of Science and Technology of China, Hefei 230026, China*

[4] *Centre of Excellence for Quantum Computation and Communication Technology, School of Physics, University of New South Wales, NSW 2052, Australia*

[5] *Centre of Excellence for Quantum Computation and Communication Technology, School of Engineering, RMIT University, Victoria 3001, Australia*

[6] *Centre of Excellence for Quantum Computation and Communication Technology, School of Physics, University of Melbourne, Victoria 3010, Australia*

(Received 18 January 2022; revised 13 June 2022; accepted 11 August 2022; published 8 September 2022; corrected 7 October 2022)

Single rare-earth ions in solids show great potential for quantum applications, including single-photon emission, quantum computing, and high-precision sensing. However, the linewidths of single rare-earth ions are often broadened due to perturbations associated with the detection methods. Identifying the dominant broadening sources is key to reduce the linewidths for practical applications. We report a spectral broadening study on a single Er^{3+} ion in a Si nanotransistor. The single ion spectra display a Lorentzian lineshape at all light intensities considered. The linewidth remains nearly constant at 32 ± 2 MHz in the low-intensity regime, and shows a monotonic increase with the intensity in the high-intensity regime. The power broadening does not persist over the microsecond time scales considered after resonant excitation. Nor does it depend on the resonant excitation intensity or the Zeeman shift. These observations and temperature-dependent measurements suggest that charge fluctuations are likely to be a dominant broadening source. Laser heating may also contribute to the power broadening. Charge suppression in the Er^{3+}-doped region and coupling Er^{3+} ions to a confined optical mode could be implemented to reduce the spectral linewidth and to enhance the sensing precision of single Er^{3+} ions in Si.

DOI: 10.1103/PhysRevApplied.18.034018

I. INTRODUCTION

Rare-earth ions in solids are promising candidates for quantum repeater and quantum memory applications due to their extraordinarily long spin-coherence times [1,2] and long optical-coherence times. Subkilohertz homogeneous linewidths of the $4f$-$4f$ transitions have been observed for rare-earth ensembles in bulk crystals via photon echo measurements [3,4], limited by decoherence processes due to magnetic or electric field fluctuations in the local environment, spin flip flops, and spin-phonon relaxation [4–6]. However, interactions between rare-earth ions and their dynamic environment cause the emission line of each ion to diffuse around an equilibrium spectral position randomly. These spectral diffusion processes impact the phase coherence for both ensemble and single rare-earth ion applications [7,8], so it is worthwhile to study and control these processes for practical applications. For instance, spin fluctuations dominate the spectral diffusion in $Er^{3+}:Y_2SiO_5$ bulk crystals via the magnetic dipole-dipole interaction [9], while charge fluctuations can play a role in the spectral diffusion observed in $Eu^{3+}:Y_2O_3$ nanoparticles [10] and similarly in semiconductor quantum dots [11,12] via the Stark effect. These interactions result in a time-dependent effective linewidth, and has been investigated for rare-earth ensembles in both bulk crystals [4,5,9,13] and nanoparticles [10,14,15].

Recent progress in the detection of single rare-earth ions promotes their potential application as single-photon emitters [8,16,17], in quantum computing [18,19], and for high-precision sensing [20]. However, the narrow $4f$-$4f$ transitions observed for ensembles correspond to excited

*Chunming@ustc.edu.cn

states with a long lifetime and weak fluorescence. As a result, the single-ion detection approaches rely on signal-enhancement methods such as single-electron charge sensing [21], utilization of higher-lying states [22–24], and coupling to a photonic cavity [8,16,17,19]. These methods inevitably introduce surface and interface states and/or strong optical fields, which may perturb the single ions or their environment, in contrast to the well-controlled bulk environment and pump-probe conditions in the ensemble experiments. The linewidths of single rare-earth ions can be broadened by these perturbations and create challenges for achieving entanglement generation and qubit operation.

Identifying the dominant broadening sources for each detection approach is key to reduce the linewidth significantly. For example, single-ion detection with an Er^{3+} : Y_2SiO_5 membrane incorporated into a Fabry-Perot cavity avoids the proximity of interfaces associated with nanophotonic cavities, and as such the homogeneous and effective linewidths are on the order of 1 and 100 kHz, respectively [8]. Also, the linewidth studies on ensemble ions in nanostructures [10,14,15,25,26] provided relevant information for optimizing the single-ion linewidths in nanostructures. For single rare-earth ions coupled to a nanophotonic cavity, lifetime-limited homogeneous linewidths have been observed [16,19], but the effective linewidths are on the order of 1–10 MHz, significantly larger than the typical values for ensemble ions in bulk crystals. Further investigation on the sources of spectral broadening [16,17,19,21,23,24] for single rare-earth ions is needed to achieve sufficiently narrow linewidths required for potential applications.

This work focuses on a single rare-earth ion detection approach using a hybrid optical-electrical method enabled by single-electron charge sensing [21]. This technique combines resonant excitation of Er^{3+} ions in the 1.54-μm telecom band with well-established nanofabrication technologies for Si-based devices. Previously observed linewidths using this hybrid technique are on the order of 10 MHz [20,21], and the spectra generally display an asymmetric lineshape attributed to a combined effect of charge accumulation and the resulting Stark shift [21]. As a result, the average electric current, from which the Er spectrum is formed, is related to the optical transition probability for the Er ion under the excitation and electrical measurement conditions used but does not represent the intrinsic excitation rate and spectral lineshape. A more recent study introduces a time-resolved single-ion detection method and opens up the possibility for a wide range of excitation conditions to be explored [27].

Here, the time-resolved method is employed to study the spectral broadening of a single Er^{3+} ion in a Si nanotransistor. The photoionization rate of a single trap induced by Er relaxation is found to be an appropriate quantity to study the spectral properties, based on both rate equation analysis and the measured intensity dependence of the photoionization rate. Spectral broadening is observed at relatively high intensities, and further experiments are performed to investigate the underlying mechanisms.

II. METHODS

The device used in this study is a Si fin-field-effect transistor (FinFET) consisting of three electrodes and a nanowire channel (35 nm width × 80 nm length × 60 nm height), as illustrated in Fig. 1(a). A small number (approximately 25) of ^{167}Er atoms (nuclear spin, $I = 7/2$) and a larger number (approximately 150) of O atoms are implanted into the device, and then the device is thermally processed to recover the implantation damage and activate the Er^{3+} ions [21].

The experiment is carried out in a closed-cycle cryostat, and the FinFET is mounted on the cold finger operating at a base temperature of 3.6 K. The FinFET is biased under a subthreshold condition [28] so that quantum dots (QDs) could form in the device channel. Current arising from the electron tunnelling through QDs is amplified by an I-V converter with a 10-kHz analog bandwidth located at room temperature. The measurement conditions allow individual Er ions to be addressed as per our earlier published work [21].

A cavity-locked laser is used to excite a single Er^{3+} ion with short-term frequency stability below 2 MHz. The long-term cavity drift is monitored with a wavemeter (Bristol 621A-NIR) to calibrate the laser frequency. The specified repeatability of the wavemeter is ±6MHz. An electro-optic modulator (EOM) is used to generate two frequency-tunable sidebands while the carrier band is suppressed to less than 0.5%. By choosing a suitable cavity resonance frequency the laser is locked to, one sideband is used to scan a well-separated Er peak for the spectral broadening study. The other sideband and the carrier band are tuned away from any Er resonances. As a result, the laser light consisted of a resonant component for the spectral scan and off-resonance components. The proportion (α) of the resonant intensity to the total intensity had a maximum value of slightly below 0.5 and could be reduced by adding off-resonance light from another laser.

Then the laser light passes through an acousto-optic modulator (AOM) for pulse generation with an extinction ratio of 50 dB and is split into two beams by a fiber-optic coupler. One beam passes through a single-mode optical fiber and is focused on the device surface with a spot size of approximately 2 μm using fiber-based confocal microscopy [29]. The other beam is sent to a photodetector for power monitoring. Unless expressly stated, the (light) intensity used in this work refers to the total light intensity on the surface of the device calculated with the monitored power and the spot size of 2 μm with $\alpha = 0.496 \pm 0.002$. Fiber polarization controllers and a fiber polarizer are used to tune the light polarization for the EOM and the device.

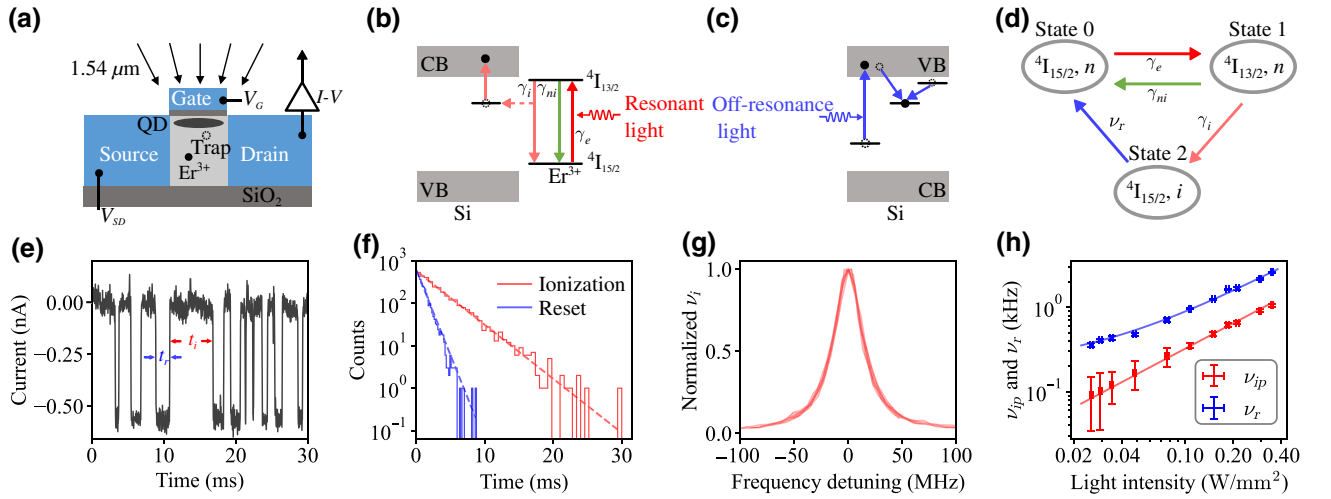

FIG. 1. Single Er^{3+} ion spectroscopy and cw measurement. (a) Cross-section schematic of the FinFET with device connection. The laser light is focused on the Er-doped channel region of the device. Energy-level diagrams showing (b) photoionization and (c) reset processes. CB and VB stand for conduction band and valence band, respectively. (d) The states and processes for building a three-state Markov chain model. (e) A short section of a typical current-time trace under resonant cw illumination. t_i and t_r represent the time intervals that it takes to ionize and reset the single trap, respectively. (f) Statistics of t_r (blue) and t_i (red) time intervals from a long time trace similar to (e). Both histograms are fitted with exponential decay functions (dashed line) and return an ionization rate, ν_i, and a reset rate, ν_r. (g) Normalized single-ion spectra measured at cw light intensities ranging from 0.025 to 0.35 W/mm^2. (h) Light-intensity dependence of the peak ionization rate ν_{ip} (red) and the reset rate ν_r (blue). Both are well fitted with a linear function (solid lines). In the low-intensity region of the logarithmic scale plot, the blue line curves due to a zero-intensity offset that corresponds to a spontaneous reset rate when no laser illumination is present.

Slow polarization drift due to the two fiber polarization controllers before the fiber polarizer led to a slight optical power fluctuation. This power fluctuation is monitored by the photodetector for each measurement and is plotted as a standard deviation in the figures.

III. RESULTS

Figures 1(b) and 1(c) show the processes involved in single-ion spectroscopy. The Er^{3+} ion is first resonantly excited from the ground state ($^4I_{15/2}$) to the excited state ($^4I_{13/2}$). At some time later it relaxes back to the ground state via either a radiative process by emitting a photon, or nonradiative processes such as Auger effect [30]. The charge ionization due to an Auger process affects the chemical potential of the QD and the tunneling current through the QD. In this device, a single trap in close proximity to the QD is ionized by Auger relaxation of the Er^{3+} ion and induces a significant change in the tunneling current. Then the ionized trap will be reoccupied (reset) by capturing an electron from a nearby reservoir or from photon-generated carriers in the channel, and consequently, the tunneling current resets to the original level.

Among the processes shown in Figs. 1(b) and 1(c), the excitation process, at a rate of γ_e, is a straightforward choice for spectral broadening and linewidth studies but is not directly observable. The two observable processes could be described by a simplified two-state Markov-chain model [27] with a photoionization rate of ν_i and a reset rate of ν_r. In this study, the photoionization rate, ν_i is used for spectral study under appropriate conditions.

To investigate the relationship between γ_e, and the photoionization rate, ν_i, a three-state Markov-chain model is built to describe all relevant processes. As shown in Fig. 1(d), the three states are state 0 : $\{^4I_{15/2}, n\}$, state 1 : $\{^4I_{13/2}, n\}$, and state 2 : $\{^4I_{15/2}, i\}$, where $^4I_{15/2}$ or $^4I_{13/2}$ stands for the electronic state of the Er^{3+} ion, and n or i stands for the neutral state or the ionized state of the single trap, respectively. These processes follow Kolmogorov's forward equation [31]:

$$\begin{bmatrix} p'_{00} & p'_{01} & p'_{02} \\ p'_{10} & p'_{11} & p'_{12} \\ p'_{20} & p'_{21} & p'_{22} \end{bmatrix} = \begin{bmatrix} p_{00} & p_{01} & p_{02} \\ p_{10} & p_{11} & p_{12} \\ p_{20} & p_{21} & p_{22} \end{bmatrix} \times \begin{bmatrix} -\gamma_e & \gamma_e & 0 \\ \gamma_e + \gamma_{ni} & -\gamma_e - \gamma_{ni} - \gamma_i & \gamma_i \\ \nu_r & 0 & -\nu_r \end{bmatrix}, \tag{1}$$

where $p_{ij} \equiv p_{ij}(t)$, is the probability that a process presently in state i will be in state j a time t later, p'_{ij} is the time derivative of p_{ij}, γ_i is the Er decay rate associated with the single-trap ionization, and γ_{ni} is the combined rate of all the other decay processes.

Here, $p_{02}(t)$ corresponds to the photoionization process in the simplified two-state Markov-chain model [27]. Its solution in the weak excitation regime (see Appendix A for details) gives

$$\nu_i \sim \frac{\gamma_i}{\gamma_i + \gamma_{ni}}\gamma_e. \tag{2}$$

This simplified solution shows that ν_i is approximately proportional γ_e as long as γ_e is well below the total decay rate, $\gamma_i + \gamma_{ni}$. The total decay rate is measured to be higher than 1 MHz (see Appendix B for details), much higher than the expected excitation rate at the relatively low intensities used in this study. Therefore, the ionization rate, ν_i, is used to represent the excitation rate in the following study. Besides, the lower bound on the total decay rate also puts a lower bound on the linewidth.

The spectral broadening study in this work is carried out in two excitation modes, cw laser excitation and pulsed laser excitation. A common side effect observed in the FinFETs is that laser illumination introduces current noise and heating, which lowers the electrical sensitivity of the current signal. In order to avoid this, cw laser excitation is used in the low-intensity regime, and pulsed laser excitation is used at high intensities. These settings ensure the observation of a large number of photoionization events within a reasonable measurement time at each laser frequency.

The spectral broadening is first investigated under cw excitation, and the intensity is limited to 0.35 W/mm^2 to maintain a sufficient signal contrast. The laser frequency is scanned over a spectral peak for each intensity, and a 20 s to 60 s current-time trace is recorded at each frequency. Figure 1(e) shows a short section of a typical time trace of current when the device is under cw resonant excitation with an intensity of 0.025 W/mm^2. The current switches between two discrete levels, and the high level and low level correspond to the occupied trap state and the ionized trap state, respectively. For each ionization-reset event, an ionization time t_i and a reset time t_r are determined as shown in Fig. 1(e). The statistics of a large number of events from a long current-time trace is plotted as the two histograms in Fig. 1(f), and both follow an exponential decay function. The fittings give an ionization rate of $\nu_i = 294(5)$Hz, and a reset rate of $\nu_r = 929(14)$Hz.

These two rates are measured as the laser scans the Er resonant peak at different intensities, and the ionization rate, ν_i, as a function of laser frequency detuning is plotted as one spectral line for each intensity in Fig. 1(g). For comparison purposes, each spectral line is normalized against its highest point and detuned in frequency against its peak position. All the spectra can be well fitted with a Lorentzian lineshape, and the fittings give a nearly constant linewidth of 32±2 MHz (full width at half maximum). The spectra with absolute ionization rates can be found in the Supplemental Material [32]. The fitted peak position fluctuates up to 15 MHz in this work without any clear dependence on the experimental conditions. This fluctuation is close to the frequency repeatability of the wavemeter and thus is not investigated further in this work.

The reset rate (blue), ν_r, and the fitted peak height, defined as the peak ionization rate (red), ν_{ip}, are plotted as a function of intensity in Fig. 1(h). The peak ionization rate is in proportion to the intensity with a slope of 3.23±0.03 kHz/(W/mm^2). This proportional relationship indicates an incoherent single-photon excitation process and verifies the conclusion in Eq. (2). The reset rate also shows a linear dependence on the intensity, besides, it does not show a wavelength dependence between 1500 nm (199.9 THz) and 1600 nm (187.3 THz). The change of the reset rate is attributed to photocarriers generated from intrabandgap states in Si due to single-photon excitation, which is expected to be dominant under 1.5-μm illumination at the low intensities used in this study [33,34]. A linear fit (blue line) of the intensity dependence of the reset rate gives a slope of 6.9±0.2 kHz/(W/mm^2), and the zero-intensity offset corresponds to a spontaneous reset rate of 0.20±0.03 kHz when no laser illumination is present [27].

The spectral broadening at higher light intensities is investigated with pulsed laser excitation. A short pulse length is chosen to ensure a negligible impact of the laser pulse on the electrical sensitivity, and there is a long time delay after the pulse for an ionization count to reset. Specifically, each measurement cycle consists of a 4-μs excitation pulse and a 5-ms dark period, as shown in the top panel of Fig. 2(a). The measurement cycle is repeated 20 000–50 000 times at each laser frequency. Then the photoionization events in all valid cycles are determined by comparing the current signal in the readout window to a threshold. Several cycles are shown in Fig. 2(a), and the current immediately before the laser pulse is subtracted from each trace as an offset. The red traces are identified as photoionization counts as the current falls below the threshold in the readout window. In contrast, the blue traces are idle cycles as the current signal remains above the threshold. Furthermore, a small proportion of traces show a below-threshold signal before the laser pulse due to an unsuccessful reset from the previous cycle, and these traces are counted as invalid cycles. Finally, the photoionization probability, defined as the ratio of photoionization counts to the total valid cycles, is calculated for each group of cycles measured under the same condition.

As shown in our previous study [27], the ionization and reset processes can be described by a two-state Markov-chain model. The photoionization probability, R, can be expressed as

$$R = \frac{\nu_i}{\nu_i + \nu_r}(1 - e^{-(\nu_i+\nu_r)t_p}), \tag{3}$$

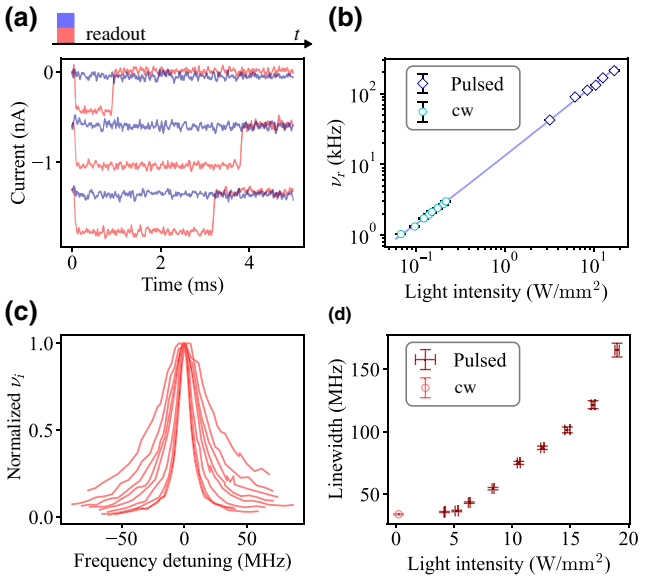

FIG. 2. Pulsed single Er^{3+} ion spectroscopy. (a) Pulse sequence and typical current-time traces. The red and blue rectangles in the laser pulse represent the resonant and off-resonance components, respectively. The three pairs of traces are offset along the y axis for clarity. The red traces with current falling below a threshold level in the readout window are identified as successful ionization counts, while the blue traces staying above the threshold are counted as idle cycles. (b) Light intensity dependence of the reset rate. The data from both cw (cyan circle) and pulsed (blue diamond) measurements follows a linear relationship (solid line) as the intensity varies by 2 orders of magnitude. (c) Normalized spectra from pulsed measurements at different intensities ranging from 4.2 to 19.0 W/mm^2. (d) Light intensity dependence of the spectral linewidth from both cw (red circle) and pulsed (dark red) measurements.

where t_p is the pulse length, and ν_r and ν_i are the reset rate and the ionization rate, respectively.

In order to calculate the ionization rate from the measured photoionization probability, the reset rate needs to be determined first. The reset rate at a high intensity can be measured with a two-pulse measurement (see Appendix C for details). The results from cw and pulsed measurements with the same experimental setup show a linear dependence of the reset rate on the light intensities [Fig. 2(b)].

Next, the ionization rate is calculated for each measured photoionization probability based on Eq. (3) and the extrapolated reset rate. Figure 2(c) shows the spectra measured at different intensities ranging from 4.2 to 19.0 W/mm^2. For comparison purposes, the ionization rates are normalized against the maximum rate at each intensity, and the same spectra with absolute ionization rates can be seen in the Supplemental Material [32]. All lines are well fitted with a Lorentzian lineshape, and the linewidths are plotted as a function of intensity in Fig. 2(d). At a low light intensity, the linewidths measured with pulsed laser excitation are close to the linewidth from the cw measurement (red circle) but start to increase as the light intensity increases up to 19.0 W/mm^2. At an even higher intensity, the signal drop due to nonresonant charge buildup [27] will intensify and affect the signal readout, and the well-separated spectral peaks at low intensities will start to overlap and affect the linewidth fitting accuracy. Therefore, the light intensity for spectral scans is limited to 19.0 W/mm^2.

Power broadening can arise from several mechanisms, such as absorption saturation at high intensities, instantaneous spectral diffusion [35–37], power-dependent dephasing or spectral diffusion processes, and an increase in temperature due to laser heating. To investigate the underlying mechanisms, several experiments are carried out.

Firstly, the spectrum is measured under different resonant proportions, α, while the total light intensity remains fixed. Figure 3(a) shows three example spectra measured with the same total intensity of 13.0 W/mm^2 but different α values. All the spectra can be well fitted with a Lorentzian lineshape. The fitted peak ionization rate and linewidth are plotted as a function of α in Fig. 3(b). The peak ionization rate increases linearly with α. In contrast, the linewidth shows no obvious trend and fluctuates around 85 MHz,

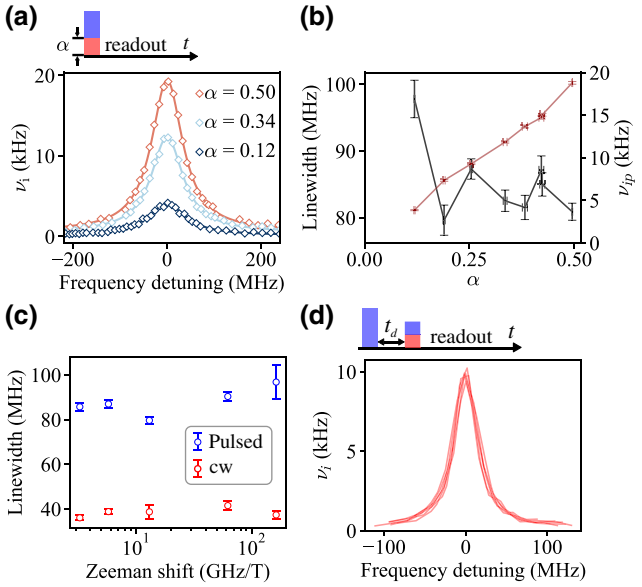

FIG. 3. Power broadening mechanism study. (a) Spectra measured with three different resonant laser pulses having the same total intensity but different proportions of the resonant light, α. (b) The dependence of the linewidth and the peak ionization rate on α. (c) Linewidths of multiple optical transitions with different Zeeman shifts. The red and blue circles are measured with 0.19 W/mm^2 cw excitation and 9.6 W/mm^2 pulsed excitation, respectively. (d) Spectra measured with different time delays, t_d, ranging from 50 ns to 10 μs. A high-intensity off-resonance laser pulse is first applied in each measurement cycle. After a time delay of t_d, a low-intensity resonant pulse is applied over a range of spectral detunings.

which is consistent with the linewidth shown in Fig. 2(d). Therefore, we conclude that the power broadening solely depends on the total intensity regardless of the resonant proportion.

Secondly, the spectral broadening is measured at spectral peaks with different Zeeman shifts, by changing the magnetic field directions and choosing either the electron spin preserving or flipping transitions. As shown in Fig. 3(c), the measured linewidths do not show an observable dependence on the Zeeman shift either at low or high intensities. This suggests that magnetic noise does not play a noticeable role in spectral broadening.

Thirdly, the persistence of the power broadening is studied with a two-pulse experiment. In each cycle, a high-intensity off-resonance laser pulse is first applied for power broadening. After a time delay of t_d, a low-intensity resonant pulse is applied to measure the Er spectrum. To create a more detectable phenomenon, the first pulse had a length of 4 μs and an intensity of 119.4 W/mm^2, more than 5 times higher than the intensity used in the power-broadening study. According to the results in Fig. 2(d), the first pulse is expected to induce a power broadening well above 150 MHz. The second pulse has an intensity of 2.9 W/mm^2, which is low enough to avoid inducing any additional broadening, and a pulse length of 4 μs to ensure a sufficient ionization count rate and a reasonable measurement time for each spectrum. Six spectra are measured with time delays ranging from 50 ns to 10 μs as shown in Fig. 3(d). All the spectra show a uniform linewidth of 34±4 MHz, consistent with the linewidth observed in Fig. 2(d) at the same intensity. (See the Supplemental Material [32] for individual spectra.) This observation indicates that the power broadening does not persist over the time scales considered.

Lastly, two additional experiments are carried out to investigate the impact of laser heating on the Er^{3+} electron spin temperature and the electron temperature in the source and drain of the FinFET.

The spin temperature of an electron spin doublet system follows Boltzmann statistics. The relative population of the $^4I_{15/2}$ spin-excited state follows,

$$p_{\mathrm{ex}} = \frac{1}{e^{\Delta E/k_B T_S} + 1}, \tag{4}$$

where ΔE is the electron Zeeman splitting, k_B is the Boltzmann constant, and T_S is the electron spin temperature. In the presence of spectral broadening, it is expected that $p_{\mathrm{ex}} \propto A_{\mathrm{peak}}/I_R$, where A_{peak} and I_R stand for the spectral peak area and resonant intensity, respectively. Spectra of the $^4I_{15/2}$ excited state are measured with cw and pulsed excitations at 0.4 T and 4.5 T with a Zeeman splitting of 142 μeV and 1.6 meV, respectively. The spin temperatures are calculated with Eq. (4) and the measured values of A_{peak}/I_R, as shown by the red markers in Fig. 4.

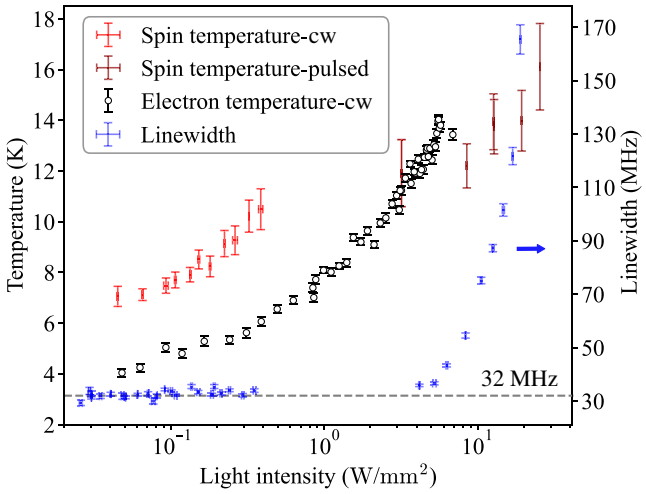

FIG. 4. Impacts of laser intensity on temperatures and the spectral linewidth. Electron spin temperatures of the Er^{3+} ion are calculated from spectra measured with cw (red) and pulsed (dark red) laser excitation. Electron temperatures (black circle) in the source and drain of the FinFET are calculated from the broadening of a Coulomb peak under off-resonance cw illumination. The linewidths presented in Figs. 1(g) and 2(d) are replotted as blue data points, and the dashed line corresponds to the minimal linewidth of 32 MHz.

The electron temperature in the source and drain of the FinFET affects the broadening of the Coulomb blockade [38]. Here, the electron temperature measurements are performed only under cw illumination, as a megahertz electrical bandwidth would be necessary to measure the transient temperature during microsecond pulses. A Coulomb peak is measured with off-resonance cw illumination at different intensities. The electron temperature is then calculated from the broadening of the Coulomb peak and plotted as the black circles in Fig. 4.

IV. DISCUSSIONS

The observed power broadening increases significantly with the total intensity but does not depend on the resonant proportion of a fixed total intensity. This suggests that the power broadening is not due to absorption saturation or frequency shifts induced by resonant excitation. The minimal linewidth and the power broadening do not show dependence on the Zeeman shift and consequently are not limited by magnetic field fluctuation due to spin flipping of nearby trap states or other Er^{3+} ions. Furthermore, these above observations rule out instantaneous spectral diffusion due to magnetic interactions.

The spectral linewidth remains approximately constant at cw light intensities up to 0.35 W/mm^2, while both the spin temperature and the electron temperature show a clear increase as the intensity increases within the same range, as shown in Fig. 4. These phenomena suggest that the minimal linewidth of 32±2 MHz is not limited by the

temperature. As the intensity further increases, the laser heating leads to a further temperature rise and can contribute to the power broadening. The Er^{3+} electron spin temperature measured with pulsed illumination would be the most relevant variable for evaluating the contribution of laser heating to the power broadening, however, the exact contribution cannot be resolved due to the limited accuracy in the relatively high spin temperature regime.

Another common source of spectral broadening is electric field perturbation arising from charge fluctuation in the channel of the FinFET. In previously measured devices, slow accumulation of electric charges could lead to asymmetrically broadened spectra [20,21] via Stark effect. In the present device, the spectral peaks display a Lorentzian lineshape, and the persistence time of the power broadening is shorter than a few microseconds. These indicate charge fluctuation in the channel of the FinFET could play a role in the power broadening. Also similar spectral diffusion processes have been reported in semiconductor quantum dots [39–41]. Since the power broadening does not show dependence on the resonant intensity, the possible sources of the charge fluctuation include photocarrier generation from intrabandgap states in Si [33,34] and ionization of traps following nonresonant excitation and relaxation of other Er^{3+} ions in the device [30,42].

In this work, the spectral scanning speed is limited by the ionization count rate to the time scale of 10 min. The spectral diffusion on this slow time scale appears smaller than 15 MHz. Further investigation on spectral diffusion on a broader range of time scales can be conducted on devices that show faster ionization rates. Correlation measurements [43] can also be used to achieve a finer time resolution.

V. CONCLUSION

In summary, we present an effective method of using the Er-induced photoionization process to investigate spectroscopic properties of a single Er^{3+} ion in Si. The ionization rate is found to be an appropriate quantity to represent the optical transition probability for spectroscopic studies, and the single-ion spectra display a Lorentzian lineshape at all light intensities in use. In the low-intensity regime, below 4.2 W/mm^2, the linewidth remains nearly constant at 32±2 MHz. The dominant broadening mechanism for this observed minimal linewidth is likely to be charge fluctuation, while temperature broadening or magnetic field fluctuation do not have significant contributions. In the high-intensity regime, between 4.2 and 19.0 W/mm^2, the linewidth increases monotonically with the total intensity, independent of the resonant intensity or the Zeeman shift. In addition, the power broadening does not persist over a few microseconds. These observations and the temperature measurements suggest that the power broadening could be caused by laser heating and charge fluctuation on a fast time scale.

This method provides a more consistent spectral lineshape than the asymmetric lineshape used in the high-precision strain measurement [20] and would enhance the strain measurement precision. However, the power broadening creates challenges for coherent experiments such as optical Rabi oscillations. Also, the observed minimum linewidth of 32±2 MHz in this device is considerably larger than the submegahertz homogeneous linewidths that have been measured for Er^{3+} ions in bulk Si [42] and in Si waveguides [26]. The charge fluctuation in the device is likely to be a dominant broadening mechanism via the Stark effect [10]. Controlled doping [44] and charge depletion [45] could be used to suppress the charge fluctuation. Furthermore, in the present devices, Er^{3+} ions are in the channel region and close to interface and trap states. This impact can be reduced in alternative device structures with a Er^{3+}-doped region separated from the channel region, and undesirable illumination on the charge-sensing device and laser heating can be further reduced by coupling the Er^{3+}-doped region to an optical cavity or waveguide.

ACKNOWLEDGMENTS

This work is supported by the National Key R&D Program of China (Grant No. 2018YFA0306600), Anhui Initiative in Quantum Information Technologies (Grant No. AHY050000), and Anhui Provincial Natural Science Foundation (Grant No. 2108085MA15).

APPENDIX A: THE Er-INDUCED IONIZATION RATE

A three-state Markov-chain model is used to simulate the excitation and relaxation processes of the Er^{3+} ion as well as the ionization and reset of the single trap, as shown in Fig. 1(d). These processes follow the Kolmogorov's forward equation, Eq. (1). The ionization process following the excitation and relaxation of the Er^{3+} ion leads to an observable signal and corresponds to the term $p_{02}(t)$ in Eq. (1).

To determine the solution for $p_{02}(t)$, the relevant equations can be transformed as

$$p_{02}(t) = \frac{p'_{00}(t) + (2\gamma_e + \gamma_{ni})p_{00}(t) - \gamma_e - \gamma_{ni}}{\nu_r - \gamma_e - \gamma_{ni}}, \tag{A1}$$

$$\begin{aligned} &p''_{00}(t) + ap'_{00}(t) + bp_{00}(t) - m = 0, \\ &a = 2\gamma_e + \gamma_{ni} + \gamma_i + \nu_r, \\ &b = \gamma_e\gamma_i + 2\gamma_e\nu_r + \gamma_{ni}\nu_r + \gamma_i\nu_r, \\ &m = \gamma_e\nu_r + \gamma_{ni}\nu_r + \gamma_i\nu_r. \end{aligned} \tag{A2}$$

Under the initial conditions of $p_{00}(0) = 1, p_{02}(0) = 0$, the solution of Eq. (A2) is

$$
\begin{aligned}
p_{00}(t) &= \frac{m}{b} + c_1 e^{-\lambda_1 t} + c_2 e^{-\lambda_2 t},\\
\lambda_1 &= \frac{a - \sqrt{a^2 - 4b}}{2},\\
\lambda_2 &= \frac{a + \sqrt{a^2 - 4b}}{2},\\
c_1 &= 1 - \frac{m}{b} - \frac{\gamma_e - \lambda_1(1 - (m/b))}{-\lambda_1 + \lambda_2},\\
c_2 &= \frac{\gamma_e - \lambda_1(1 - (m/b))}{-\lambda_1 + \lambda_2}.
\end{aligned}
\tag{A3}
$$

$p_{02}(t)$ is then derived from Eqs. (A1) and (A3) as

$$
p_{02}(t) = \frac{\gamma_e \gamma_i}{b} + \frac{c_1(2\gamma_e + \gamma_{ni} - \lambda_1)e^{-\lambda_1 t} + c_2(2\gamma_e + \gamma_{ni} - \lambda_2)e^{-\lambda_2 t}}{\nu_r - \gamma_e - \gamma_{ni}}. \tag{A4}
$$

In the weak excitation regime, the following condition is satisfied, $\gamma_e, \nu_r \ll \gamma_i, \gamma_{ni}$. The time dependence of $p_{02}(t)$ is then dominated by the first exponential decay term with a time constant of $1/\lambda_1$. Compared to Eq. (3) in the main text, the ionization rate can be expressed as

$$
\begin{aligned}
\nu_i &= \lambda_1 - \nu_r\\
&= \frac{a - \sqrt{a^2 - 4b}}{2} - \nu_r\\
&\sim \frac{b}{a} - \nu_r\\
&= \frac{\gamma_e \gamma_i - \nu_r^2}{2\gamma_e + \gamma_{ni} + \gamma_i + \nu_r}\\
&\sim \frac{\gamma_i}{\gamma_i + \gamma_{ni}} \gamma_e.
\end{aligned}
\tag{A5}
$$

Thus at low light intensities, the ionization rate in the two-state Markov-chain model, ν_i, is approximately proportional to the excitation rate, γ_e.

APPENDIX B: DECAY TIME OF THE Er EXCITED STATE

Due to the electric bandwidth limitation (10 kHz), the decay time of the $^4I_{13/2}$ excited state cannot be measured accurately in this work. However, an upper bound of the decay time can be determined from the variation of the signal transition time after a short excitation pulse [27]. Figure 5(a) shows multiple current-time traces after a 1-μs resonant pulse. Each current trace is fitted to a step function, and a signal transition time, i.e., the start time of the falling edge, is extracted. A histogram of all signal transition times is plotted in Fig. 5(b) and is fitted to a Gaussian function and an exponential-Gaussian

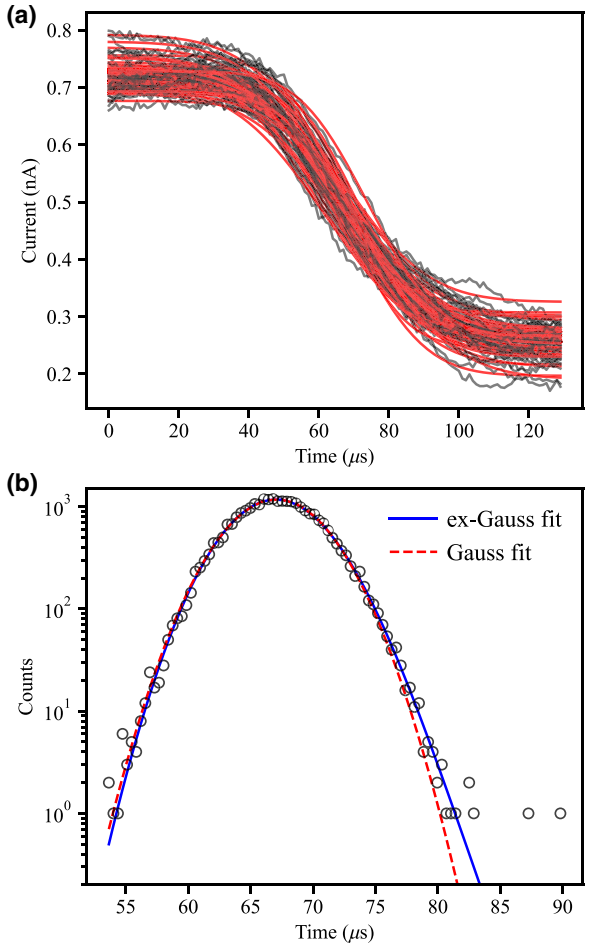

FIG. 5. Decay time of the $^4I_{13/2}$ excited state. (a) Pulse sequence and example current-time traces from successful ionization cycles. (b) A histogram of all current switching times, fitted to an exponential-Gaussian function (solid line) and a Gaussian function (dashed line).

function. The histogram well follows a Gaussian distribution, consistent with the previous observation [27]. The exponential-Gaussian fitting gives a decay time of 0.72 ± 0.10 μs. Additionally, the 1-μs pulse length also sets an upper bound on the detectable decay time. Therefore, these results set an upper bound of 1 μs on the decay time of the Er^{3+} $^4I_{13/2}$ state.

APPENDIX C: THE LIGHT-ASSISTED RESET RATE

The pulse sequence is shown on the top section of Fig. 6. A resonant pulse is first applied in each cycle to generate photoionization events. The current signal in the "first readout" window is compared against a threshold level to determine whether there is an ionization count. At the end of the "first readout" window, an off-resonance pulse is applied to reset any ionization signal. Whenever an ionization count appears in the "first readout" window of a cycle, the current signal in the beginning of the "second readout" window is compared against the threshold level to determine if the ionization count has been reset by the end of the second laser pulse. The ratio of the remaining counts in the beginning of the "second readout" window to the counts that appear in the "first readout" window is defined as the remaining count probability. This measurement is carried out with different lengths and optical intensities of the second pulse. As shown in Fig. 6, the remaining count probability drops exponentially as the second-pulse length increases. Each colored line represents an exponential decay fit of the results under one second-pulse intensity. The fitted reset rates are shown in Fig. 2(b) in the main paper.

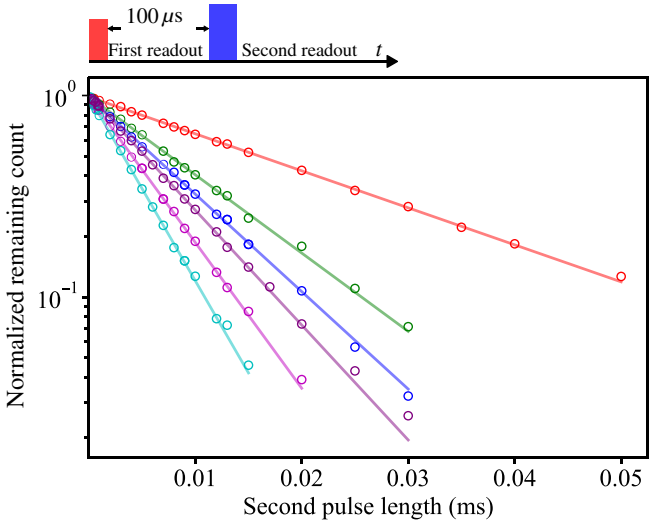

FIG. 6. Light-assisted reset. Pulse sequence (top panel) and normalised remaining counts after the second pulse in the two-pulse experiments. The data points and fittings for different second pulse intensities are plotted in different colours.

[1] M. Zhong, M. P. Hedges, R. L. Ahlefeldt, J. G. Bartholomew, S. E. Beavan, S. M. Wittig, J. J. Longdell, and M. J. Sellars, Optically addressable nuclear spins in a solid with a six-hour coherence time, Nature **517**, 177 (2015).

[2] M. Rančić, M. P. Hedges, R. L. Ahlefeldt, and M. J. Sellars, Coherence time of over a second in a telecom-compatible quantum memory storage material, Nat. Phys. **14**, 50 (2018).

[3] T. Böttger, C. W. Thiel, R. L. Cone, and Y. Sun, Effects of magnetic field orientation on optical decoherence in Er^{3+} : Y_2SiO_5, Phys. Rev. B **79**, 115104 (2009).

[4] R. Fukumori, Y. Huang, J. Yang, H. Zhang, and T. Zhong, Subkilohertz optical homogeneous linewidth and dephasing mechanisms in Er^{3+} : Y_2O_3, Phys. Rev. B **101**, 214202 (2020).

[5] C. W. Thiel, N. Sinclair, W. Tittel, and R. L. Cone, Optical decoherence studies of Tm^{3+} : $Y_3Ga_5O_{12}$, Phys. Rev. B **90**, 214301 (2014).

[6] N. Kunkel, J. Bartholomew, S. Welinski, A. Ferrier, A. Ikesue, and P. Goldner, Dephasing mechanisms of optical transitions in rare-earth-doped transparent ceramics, Phys. Rev. B **94**, 184301 (2016).

[7] F. K. Asadi, S. C. Wein, and C. Simon, Protocols for long-distance quantum communication with single ^{167}Er ions, Quantum Sci. Technol. **5**, 045015 (2020).

[8] A. Ulanowski, B. Merkel, and A. Reiserer, Spectral multiplexing of telecom emitters with stable transition frequency, ArXiv:2110.09409 (2021).

[9] T. Böttger, C. W. Thiel, Y. Sun, and R. L. Cone, Optical decoherence and spectral diffusion at 1.5 μm in Er^{3+} : Y_2SiO_5 versus magnetic field, temperature, and Er^{3+} concentration, Phys. Rev. B **73**, 075101 (2006).

[10] J. G. Bartholomew, K. de Oliveira Lima, A. Ferrier, and P. Goldner, Optical line width broadening mechanisms at the 10 kHz level in Eu^{3+} : Y_2O_3 nanoparticles, Nano Lett. **17**, 778 (2017).

[11] V. Türck, S. Rodt, O. Stier, R. Heitz, R. Engelhardt, U. W. Pohl, D. Bimberg, and R. Steingrüber, Effect of random field fluctuations on excitonic transitions of individual CdSe quantum dots, Phys. Rev. B **61**, 9944 (2000).

[12] J. Seufert, R. Weigand, G. Bacher, T. Kümmell, A. Forchel, K. Leonardi, and D. Hommel, Spectral diffusion of the exciton transition in a single self-organized quantum dot, Appl. Phys. Lett. **76**, 1872 (2000).

[13] L. Veissier, M. Falamarzi, T. Lutz, E. Saglamyurek, C. W. Thiel, R. L. Cone, and W. Tittel, Optical decoherence and spectral diffusion in an erbium-doped silica glass fiber featuring long-lived spin sublevels, Phys. Rev. B **94**, 195138 (2016).

[14] D. Serrano, J. Karlsson, A. Fossati, A. Ferrier, and P. Goldner, All-optical control of long-lived nuclear spins in rare-earth doped nanoparticles, Nat. Commun. **9**, 2127 (2018).

[15] B. Casabone, J. Benedikter, T. Hümmer, F. Oehl, K. d. O. Lima, T. W. Hänsch, A. Ferrier, P. Goldner, H. d. Riedmatten, and D. Hunger, Cavity-enhanced spectroscopy of a few-ion ensemble in Eu^{3+} : Y_2O_3, New J. Phys. **20**, 095006 (2018).

[16] T. Zhong, J. M. Kindem, J. G. Bartholomew, J. Rochman, I. Craiciu, V. Verma, S. W. Nam, F. Marsili, M. D. Shaw,

A. D. Beyer, and A. Faraon, Optically Addressing Single Rare-Earth Ions in a Nanophotonic Cavity, Phys. Rev. Lett. **121**, 183603 (2018).

[17] A. M. Dibos, M. Raha, C. M. Phenicie, and J. D. Thompson, Atomic Source of Single Photons in the Telecom Band, Phys. Rev. Lett. **120**, 243601 (2018).

[18] M. Raha, S. Chen, C. M. Phenicie, S. Ourari, A. M. Dibos, and J. D. Thompson, Optical quantum nondemolition measurement of a single rare earth ion qubit, Nat. Commun. **11**, 1605 (2020).

[19] J. M. Kindem, A. Ruskuc, J. G. Bartholomew, J. Rochman, Y. Q. Huan, and A. Faraon, Control and single-shot readout of an ion embedded in a nanophotonic cavity, Nature **580**, 201 (2020).

[20] Q. Zhang, G. Hu, G. G. de Boo, M. Rančić, B. C. Johnson, J. C. McCallum, J. Du, M. J. Sellars, C. Yin, and S. Rogge, Single rare-earth ions as atomic-scale probes in ultrascaled transistors, Nano Lett. **19**, 5025 (2019).

[21] C. Yin, M. Rancic, G. G. de Boo, N. Stavrias, J. C. McCallum, M. J. Sellars, and S. Rogge, Optical addressing of an individual erbium ion in silicon, Nature **497**, 91 (2013).

[22] R. Kolesov, K. Xia, R. Reuter, R. Stöhr, A. Zappe, J. Meijer, P. Hemmer, and J. Wrachtrup, Optical detection of a single rare-earth ion in a crystal, Nat. Commun. **3**, 1029 (2012).

[23] T. Utikal, E. Eichhammer, L. Petersen, A. Renn, S. Götzinger, and V. Sandoghdar, Spectroscopic detection and state preparation of a single praseodymium ion in a crystal, Nat. Commun. **5**, 3627 (2014).

[24] K. Xia, R. Kolesov, Y. Wang, P. Siyushev, T. Kornher, R. Reuter, S. Yang, and J. Wrachtrup, Spectroscopy properties of a single praseodymium ion in a crystal, New J. Phys. **22**, 073002 (2020).

[25] D. Serrano, S. K. Kuppusamy, B. Heinrich, O. Fuhr, D. Hunger, M. Ruben, and P. Goldner, Ultra-narrow optical linewidths in rare-earth molecular crystals, Nature **603**, 241 (2022).

[26] A. Gritsch, L. Weiss, J. Früh, S. Rinner, and A. Reiserer, Narrow optical transitions in erbium-implanted silicon waveguides, ArXiv:2108.05120 (2021).

[27] G. Hu, G. G. de Boo, B. C. Johnson, J. C. McCallum, M. J. Sellars, C. Yin, and S. Rogge, Time-resolved photoionization detection of a single Er^{3+} ion in silicon, Nano Lett. **22**, 396 (2022).

[28] H. Sellier, G. P. Lansbergen, J. Caro, S. Rogge, N. Collaert, I. Ferain, M. Jurczak, and S. Biesemans, Subthreshold channels at the edges of nanoscale triple-gate silicon transistors, Appl. Phys. Lett. **90**, 073502 (2007).

[29] A. Högele, S. Seidl, M. Kroner, K. Karrai, C. Schulhauser, O. Sqalli, J. Scrimgeour, and R. J. Warburton, Fiber-based confocal microscope for cryogenic spectroscopy, Rev. Sci. Instrum. **79**, 023709 (2008).

[30] A. Kenyon, Erbium in silicon, Semicond. Sci. Technol **20**, R65 (2005).

[31] S. M. Ross, in *Introduction to Probability Models*, edited by S. M. Ross (Academic Press, London, 2019) 12th ed., p. 375.

[32] See the Supplemental Material at http://link.aps.org/supplemental/10.1103/PhysRevApplied.18.034018 for the spectra with absolute ionization rates.

[33] A. D. Bristow, N. Rotenberg, and H. M. van Driel, Two-photon absorption and Kerr coefficients of silicon for 850–2200 nm, Appl. Phys. Lett. **90**, 191104 (2007).

[34] A. Gil-Molina, I. Aldaya, J. L. Pita, L. H. Gabrielli, H. L. Fragnito, and P. Dainese, Optical free-carrier generation in silicon nano-waveguides at 1550 nm, Appl. Phys. Lett. **112**, 251104 (2018).

[35] J. Huang, J. M. Zhang, A. Lezama, and T. W. Mossberg, Excess Dephasing in Photon-Echo Experiments Arising from Excitation-Induced Electronic Level Shifts, Phys. Rev. Lett. **63**, 78 (1989).

[36] G. K. Liu and R. L. Cone, Laser-induced instantaneous spectral diffusion in Tb^{3+} compounds as observed in photon-echo experiments, Phys. Rev. B **41**, 6193 (1990).

[37] J. Dajczgewand, R. Ahlefeldt, T. Böttger, A. Louchet-Chauvet, J.-L. L. Gouët, and T. Chanelière, Optical memory bandwidth and multiplexing capacity in the erbium telecommunication window, New J. Phys. **17**, 023031 (2015).

[38] L. P. Kouwenhoven, C. M. Markus, P. L. McEuen, S. Tarucha, R. M. Westervelt, and N. S. Wingreen, *Electron Transport in Quantum Dots*, NATO ASI Series E Applied Sciences, Vol. 345 (Advanced Study Institute, 1997), p. 105.

[39] S. A. Empedocles, D. J. Norris, and M. G. Bawendi, Photoluminescence Spectroscopy of Single CdSe Nanocrystallite Quantum Dots, Phys. Rev. Lett. **77**, 3873 (1996).

[40] H. D. Robinson and B. B. Goldberg, Light-induced spectral diffusion in single self-assembled quantum dots, Phys. Rev. B **61**, R5086 (2000).

[41] M. Abbarchi, F. Troiani, C. Mastrandrea, G. Goldoni, T. Kuroda, T. Mano, K. Sakoda, N. Koguchi, S. Sanguinetti, A. Vinattieri, and M. Gurioli, Spectral diffusion and line broadening in single self-assembled GaAs/AlGaAs quantum dot photoluminescence, Appl. Phys. Lett. **93**, 162101 (2008).

[42] I. R. Berkman, A. Lyasota, G. G. de Boo, J. G. Bartholomew, B. C. Johnson, J. C. McCallum, B.-B. Xu, S. Xie, R. L. Ahlefeldt, M. J. Sellars, C. Yin, and S. Rogge, Sub-megahertz homogeneous linewidth for Er in Si via in situ single photon detection, ArXiv:2108.07090 (2021).

[43] G. Sallen, A. Tribu, T. Aichele, R. André, L. Besombes, C. Bougerol, M. Richard, S. Tatarenko, K. Kheng, and J.-P. Poizat, Subnanosecond spectral diffusion measurement using photon correlation, Nat. Photonics **4**, 696 (2010).

[44] D. R. Candido and M. E. Flatté, Suppression of the Optical Linewidth and Spin Decoherence of a Quantum Spin Center in a *p*-*n* Diode, PRX Quantum **2**, 040310 (2021).

[45] C. P. Anderson, A. Bourassa, K. C. Miao, G. Wolfowicz, P. J. Mintun, A. L. Crook, H. Abe, J. U. Hassan, N. T. Son, T. Ohshima, and D. D. Awschalom, Electrical and optical control of single spins integrated in scalable semiconductor devices, Science **366**, 1225 (2019).

Correction: The abbreviation for fin-field-effect transistor (FinFET) was set incorrectly throughout the paper during the production cycle and has been fixed.